Understanding and Predicting Bubble Growth in Bubbling Fluidized Beds via Physics-Aware Data-Driven Models

Citation for the original published paper (version of record):
Chew, J., Andersson, R., Cocco, R. (2026). Understanding and Predicting Bubble Growth in
Bubbling Fluidized Beds via Physics-Aware
Data-Driven Models. Industrial & Engineering Chemistry Research, 65(13): 7273-7286.
http://dx.doi.org/10.1021/acs.iecr.5c05433

I&EC research
Industrial & Engineering Chemistry Research

pubs.acs.org/IECR
Article

Understanding and Predicting Bubble Growth in Bubbling Fluidized Beds via Physics-Aware Data-Driven Models

Jia Wei Chew,* Ronnie Andersson, and Ray A. Cocco

Cite This: *Ind. Eng. Chem. Res.* 2026, 65, 7273−7286

Read Online

ACCESS | Metrics & More | Article Recommendations

ABSTRACT: Bubble dynamics in bubbling fluidized bed reactors govern heat and mass transfer rates, mixing uniformity, and overall process efficiency, but remain challenging to predict accurately. This study develops a hybrid modeling framework to model bubble growth along bed height by integrating empirical correlations with data-driven corrections using Physics-Informed Neural Networks (PINNs) and Universal Differential Equations (UDEs). Experimental data used for training, which were obtained for Geldart Group B particles with various particle size distributions (PSDs), are characteristically noisy with non-normal bubble diameter distributions. The optimal black-box data-driven NN fails to capture the known monotonic bubble growth with bed height. In contrast, the PINN, embedding the Hilligardt−Werther empirical correlation, enforces physical monotonicity and robustness despite the noisy data. The UDE further couples this empirical correlation with a learned neural correction, yielding a physically interpretable, data-calibrated model. Results show that the UDE preserves the physical trend while adaptively compensating for empirical correlation discrepancies, with the data-driven neural correction contributing 20−35% of the total trend. The largest data-driven correction occurs for the broadest PSD case, which is expected because such conditions likely lie outside the calibration range of the empirical correlation. Importantly, this also demonstrates the ability of the hybrid framework to extend empirical models beyond their original scope. In the absence of first-principles-based descriptions, the hybrid (gray-box) approach presented here reconciles physical underpinnings with data-driven flexibility, offering a more reliable, interpretable, and generalizable framework for modeling bubble growth in practical fluidized beds.

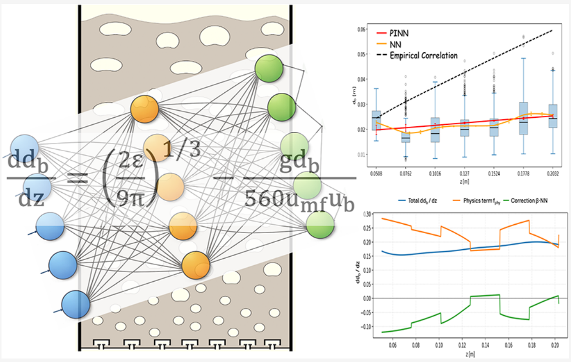

1. INTRODUCTION

Fluidized-bed reactors underpin a wide range of thermal and reactive processes, including catalytic cracking, combustion, gasification, pyrolysis, reduction, coating, and granulation, because they deliver high gas−solid contact, rapid heat and mass transfer, and scalable mixing characteristics.[1] Among the fluidization regimes, the bubbling fluidized bed (BFB) has important implications, historically central to combustion and gasification technologies and still widely used in energy and chemical manufacturing.[2,3] Reviews have highlighted that the design, operation, and scale-up of BFBs remain challenging, primarily because the underlying bubbling hydrodynamics and associated heat-transfer mechanisms are not yet fully understood.[4,5] Traditional and emerging bubbling fluidized bed applications underscore the need for more reliable, physics-consistent models to accelerate design and optimization.

In a BFB, the formation, coalescence, breakup and ascent of gas bubbles within the solid-particle matrix govern the bed's hydrodynamics and, consequently, key performance metrics such as mass transfer, heat transfer, and mixing efficiency. Bubbles generally rise in the dense phase, promoting rapid recirculation of particles in their wake, enhancing gas−solid contact, and disrupting stagnation zones, thus ensuring approximately uniform temperatures even at the industrial scale. At the mesoscale, bubbles act as large coherent structures that govern entrainment, solids mixing and emulsion dynamics, with multiscale analyses of fine-particle beds showing that bubble-cloud behaviors dominate the fluctuation and energy fraction of the flow.[6] Consequently, accurate prediction of bubble size distribution, rise velocity and spatial evolution is critical. Bubbles are not just incidental features of fluidization but are fundamental drivers of bed behavior, making their characterization a necessary step in improving the understanding, prediction and operation of BFBs.

Bubbles have been characterized for decades using experiments, correlations, and increasingly detailed measurements

Received: December 31, 2025
Revised: March 16, 2026
Accepted: March 17, 2026
Published: March 25, 2026

https://doi.org/10.1021/acs.iecr.5c05433

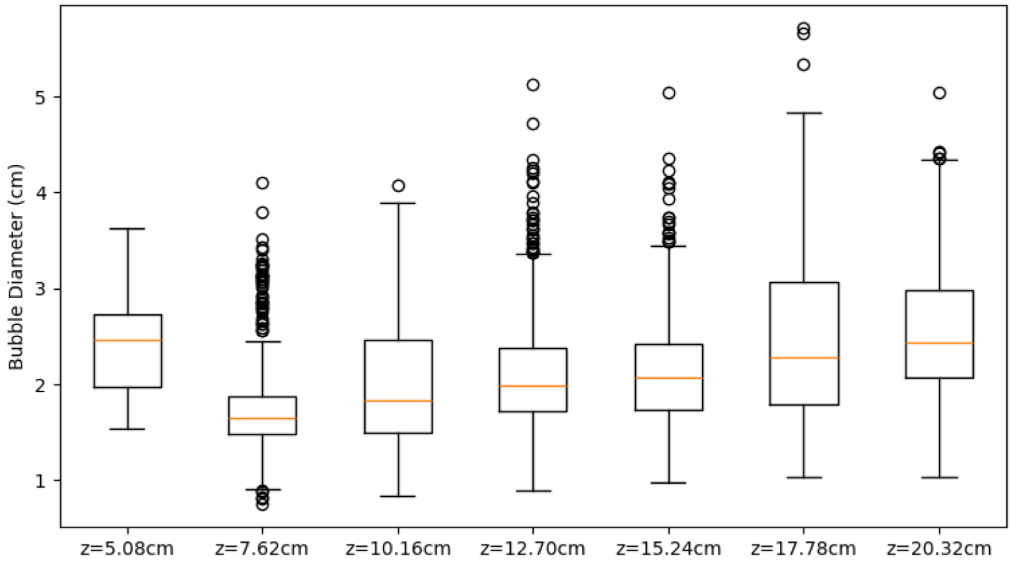

Figure 1. Box and whisker plots of bubble diameters at seven heights along the bubbling fluidized bed. Adapted with permission.[34] Copyright 2011 Wiley.

and simulations.[7] Improved measurement techniques have greatly expanded what can be resolved in opaque beds. Recent reviews detail advances in sensors and potential for hybridizing with machine learning techniques,[8] progress in X-ray imaging techniques for delivering time-resolved voidage maps and bubble property distributions without disturbing hydrodynamics,[9] as well as enhanced electrical capacitance tomography enabling 3D, high-speed tracking.[10] Recent computational fluid dynamics (CFD) reviews highlight the growing capability of simulations to capture bubble formation, growth, and breakup in gas−solid fluidized beds. A recent review of drag models and mesoscale structure corrections in pressurized bubbling systems identifies how unmodified two-fluid models tend to overestimate bed expansion and mispredict bubble behavior.[11] Studies comparing computational fluid dynamics-discrete element method (CFD-DEM) results with experiments demonstrate that capturing broader bubble size distributions and strong sensitivity to bed geometry, particle size distribution and operating conditions remain challenges.[12,13]

Classical empirical correlations generally link bubble characteristics with parameters like gas velocity, particle size and bed height. The early ones include those of Davidson[14] that describe bubble growth with height due to coalescence. Mori and Wen proposed a correlation that incorporates bed-diameter effects via a coalescence-limited maximum bubble size, improving estimates across column sizes.[15] Horio and Nonaka[16] developed a correlation applicable across Geldart particle groups, accounting for the presence and lack of a maximum bubble size characteristic of respectively Groups A and B. Werther refined correlations for bubble size, local gas holdup, and bed expansion based on large-diameter beds and capacitance-probe measurements.[17] More recent evaluations compare and stress-test these correlations across particle classes and scales,[7,18] while high-speed imaging, computer vision, and deep learning now quantify bubble size distributions and rise velocities with improved automation and resolution.[8,19] Computational studies continue to benchmark predictions against canonical correlations,[22,23] but discrepancies rooted in inadequate accounting of coalescence, breakup, and direct wall interactions[24] are well-acknowledged.

Nonetheless, important gaps remain. Empirical correlations were generally calibrated on narrow PSDs or specific regimes and exhibit deteriorating accuracy when applied to broad or multimodal PSDs. Systematic evaluations report large, operating condition-dependent errors outside their calibration ranges.[25,26] Moreover, such empirical forms rarely encode physical constraints (e.g., bounds, monotonicity, asymptotics), which can exacerbate bias under noisy measurements or extrapolations beyond the tested scope.[7] Conversely, purely data-driven models (black-box neural networks) can fit complex trends,[27,28] yet risk nonphysical behavior and limited interpretability. To this end, physics-informed machine learning offers a middle path: physics-informed neural networks (PINNs) embed governing equations into the loss to regularize learning, while universal differential equations (UDEs) augment mechanistic ODEs/PDEs with learned correction terms so that known physics and data cotrain within one model.[29] Since PINNs were introduced as a hybrid physics-aware framework a few years ago,[30] the ability to marry physics and data has received widespread interest, since all processes are inevitably governed by physical constraints.

Recent studies demonstrate the promise of such hybrid approaches in fluidization systems. Physics-informed and augmented neural networks have been applied to gas−solid reactors to improve interpretability and predictive robustness relative to purely mechanistic or purely data-driven models.[31,32] In parallel, machine-learning-assisted experimental analyses, including deep-learning-based bubble segmentation, automated tracking, and data-driven characterization of bubble dynamics, have significantly improved the resolution and reproducibility of bubble measurements in fluidized beds.[19,20,33] These advances underscore the growing synergy between experimental measurements and physics-aware learning frameworks for diagnosing and modeling complex bubbling hydrodynamics.

This study develops and validates a hybrid, physics-aware model of bubble growth in a bubbling fluidized bed that (i) employs a PINN model to enforce physically consistent trends,

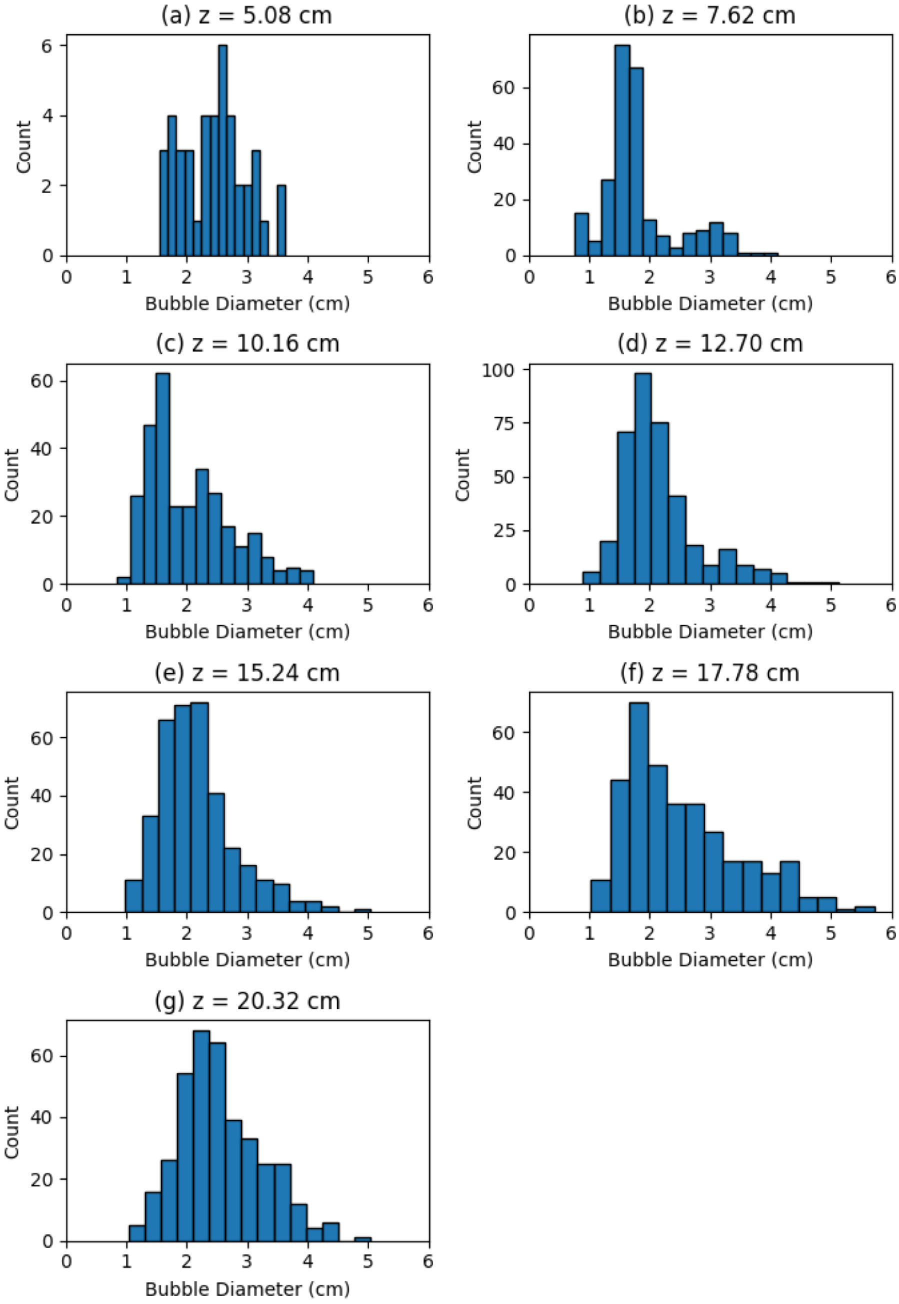

Figure 2. Distributions of bubble diameters at seven heights along the bubbling fluidized bed. Adapted with permission.[34] Copyright 2011 Wiley.

and (iii) advances a UDE formulation that couples the Hilligardt–Werther-type empirical correlation[17] with a learned neural correction, training both empirical constants and correction weights from data. The UDE model's rebalancing of physics and learning as the PSD broadens is quantified using derivative decompositions and global/local sensitivity analyses to assess interpretability and robustness. In the persistent absence of first-principles-based descriptions, this analysis establishes a pathway toward physically consistent, data-calibrated prediction of bubble size evolution that remains reliable even when constrained to empirical correlations and noisy data.

2. DATA SET

Figures 1 and 2 summarize the bubble diameters (d_b), measured using a fiber-optic probe, at seven heights (z) along the bubbling fluidized bed (BFB).[34] At each height, bubble characteristics were measured at nine radial positions, and all radial measurements were included in the reported statistics at that elevation; radial variations were comparatively small relative to axial changes, so the present analysis focuses on axial evolution. The fluidization column had an inner diameter of 18.5 cm, and a sintered metal plate at the bottom that serves as a distributor plate. The particles are largely Geldart Group B, namely, sand with a Sauter-mean particle diameter of 375 μm, and varying particle size distributions (PSDs). Data from all seven experimentally investigated PSD cases are included in Figures 1 and 2, comprising Gaussian PSDs with ratios of standard deviation to Sauter-mean particle diameter (σ/d_{sm}) ranging from 10 to 30% and log-normal PSDs with σ/d_{sm} ranging from 10 to 70%. The superficial gas velocity used was 1.2 times of the complete fluidization

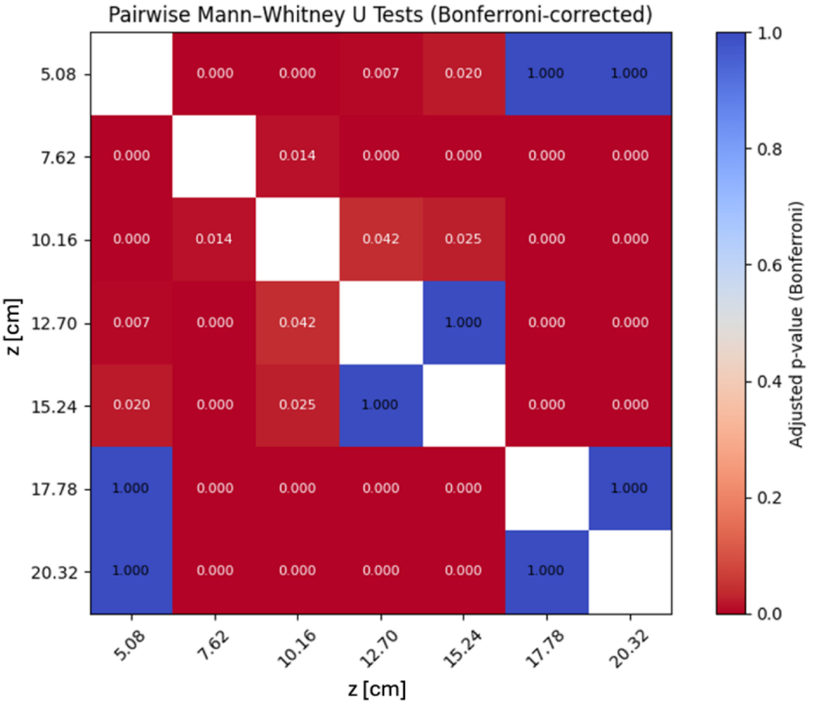

Figure 3. Heat map of cross-correlation between the bubble diameter distributions at the different heights. Red denotes statistically different ($p < 0.05$), while blue denotes statistically similar.

velocity. Although the operating condition is limited to a single gas velocity, the range of PSD widths provides a compelling set of test cases for challenging and evaluating the models.

The boxplots in Figure 1 provide an overview of the spreads and medians of d_b across heights (z) ranging from 5.08 to 20.32 cm. Along the bed height, the median bubble diameter generally increases, though the data exhibit substantial variability and skewness. The corresponding histograms in Figure 2 reveal that the bubble size distributions at all heights deviate significantly from normality, with most showing multimodal or right-skewed shapes. These non-normal features suggest the coexistence of multiple bubble populations resulting from dynamic coalescence and breakup occurrences within the heterogeneous flow field.

A nonparametric Kruskal–Wallis test confirmed that the d_b distributions differ significantly across bed heights ($H = 272.9$, $p = 5.1 \times 10^{-56}$), indicating that bubble behavior evolves systematically with axial position. Pairwise comparisons further revealed that nearly all height pairs exhibit statistically significant differences ($p < 0.05$, corrected for multiple testing), except for a few adjacent levels with overlapping variability. For instance, the mean bubble diameter increased from approximately 1.82 cm at $z = 7.62$ to 2.55 cm at $z = 20.32$ cm, while the standard deviation also grew from 0.61 to 0.69 cm, reflecting enhanced bubble size dispersion at higher elevations. These results are consistent with the physical expectation that bubbles coalesce and expand as they rise through the bed, driven by hydrodynamic instabilities.

Figure 3 presents the results of a pairwise statistical comparison of bubble-diameter distributions across the measured heights. The predominance of red cells ($p < 0.05$) indicates that bubble-size distributions differ significantly between most height pairs, confirming axial evolution of the bubble population. A small number of blue cells ($p = 1.000$) indicate height pairs for which the distributions are not statistically distinguishable, suggesting that changes between those particular elevations are small relative to measurement variability. Overall, the results substantiate that bubble size varies with height, providing a rigorous basis for subsequent data-driven and physics-informed modeling.

The statistical characterization of bubble sizes across the fluidized bed height establishes a clear physical foundation for model development. The observed general increase in bubble diameter, accompanied by non-normal and heteroskedastic distributions, confirms that bubble dynamics in the bed are inherently nonlinear and spatially dependent. These non-idealities highlight the limitations of purely empirical correlations in capturing the complex evolution of bubble populations, especially under varying hydrodynamic and particle-size distributions. Consequently, the analysis in this study employs physics-informed hybrid modeling approaches, namely, the Physics-Informed Neural Network (PINN) and Universal Differential Equation (UDE) frameworks, to incorporate known physical governance while retaining the flexibility needed to integrate data-driven corrections. Together, these methods aim to reconcile the deterministic structure of bubble growth physics with the stochastic variability revealed by the experimental measurements.

3. METHODOLOGY

All models were implemented in Python. All neural components were constructed as fully connected feedforward networks (multilayer perceptrons) and trained using the Adam optimizer.

Experimental data (namely, measurement height z, bubble diameter d_b, voidage ε, bubble velocity u_b) were converted to consistent SI units prior to training. For numerical stability, input variables were standardized to zero mean and unit variance where used in neural-network components. For the purely data-driven neural network (NN), both z and d_b were standardized, and predictions were subsequently transformed back to physical units. For the physics-informed neural network (PINN), the same standardization was applied; however, derivatives computed via automatic differentiation in normalized coordinates were converted back to dimensional form using the chain rule so that the governing differential equation was enforced consistently in physical units. In the universal differential equation (UDE) formulation, $d_b$was retained in physical units, while z, ε, and u_b were standardized when used as inputs to the neural correction term to ensure balanced learning across variables. As in the PINN, derivatives with respect to the normalized coordinate were mapped to physical space via the chain rule. In all cases, normalization was used solely for numerical stability and did not alter the structure or physical interpretation of the empirical correlation or governing equations.

The initial condition was specified differently given the distinct roles of constraint anchoring in the PINN versus joint parameter learning in UDE. In the PINN, the bubble diameter at the lowest measurement height was included through an initial-condition penalty term; defining the initial condition as the mean d_b value at $z = 0.0508$ m was found to improve stability and run-to-run reproducibility. In contrast, the UDE formulation jointly optimizes the empirical term and neural correction term under a global objective; accordingly, the initial condition is enforced more softly as part of the overall fit. In the present implementation, the UDE initial value was taken as the first recorded measurement in the data set when $z = 0.0508$ m, which may introduce a small offset in the predicted starting point relative to the PINN while preserving the inferred axial growth behavior and physics-data decomposition.

A fixed random 80:20 train:validation split was used for the purely data-driven NN to mitigate overfitting. The split was generated once per run and held fixed throughout training. The training and validation losses were monitored to assess generalization performance, and early stopping retained the model state corresponding to the minimum validation loss. In contrast, the PINN and UDE models were trained using composite objectives including data-fit, physics-residual, and initial-condition terms, and were primarily assessed based on physically consistent trends and stability of the learned differential balance. For the PINN and UDE, the physics residual was enforced at collocation points along the bed height using automatic differentiation.

Convergence was assessed by monitoring the objective function during training. For the NN and PINN, a patience-based early stopping criterion retained the model state corresponding to the minimum validation or data-fit loss. For the UDE, the composite loss (data, physics-residual, and initial-condition terms) decreased and reached a stable plateau during training, with learned parameters converging to steady values.

Hyperparameters for the NN and PINN models were selected via repeated random search over predefined discrete ranges. For the NN, the search space included network depth (2−4 layers), hidden-layer width (32−192 neurons), activation function (tanh or ReLU), learning rate (1×10^{-3}, 5×10^{-4}, 2×10^{-4}), and L_2 weight decay (0, 1×10^{-4}, 1×10^{-3}). For the PINN, the search space included network depth (3−5 layers), hidden-layer width (32−128 neurons), activation function (tanh or GELU), learning rate (1×10^{-3}, 5×10^{-4}, 1×10^{-4}), and the relative weights of the physics-residual ($w_{\text{phys}} \in \{1, 3, 5\}$) and initial-condition ($w_{\text{ic}} \in \{0.01, 0.025, 0.05\}$) penalties. In contrast, the UDE model was implemented with a fixed neural-correction architecture and fixed training settings to limit additional tuning degrees of freedom and to emphasize interpretability of the physics−data decomposition. Specifically, the correction network used a three-layer multilayer perceptron with 64 neurons per layer and tanh activation, trained with Adam (learning rate 1×10^{-3}, weight decay 1×10^{-6}) for 4000 epochs using a SmoothL1 (Huber) objective combining data-fit, physics-residual, and initial-condition terms ($w_{\text{data}} = 1$, $w_{\text{phys}} = 10$, $w_{\text{ic}} = 1$).

To assess robustness with respect to initialization and optimization variability, each final model configuration was trained three times with different random initializations, and reported results represent the mean and standard deviation across repeated runs.

4. MODEL DEVELOPMENT, RESULTS, AND DISCUSSION

The empirical correlation used as the governing equation for bubble growth with bed height is the one presented by Hilligardt and Werther in 1987:[17]

$$\frac{\mathrm{d}d_b}{\mathrm{d}z} = \left(\frac{2\varepsilon}{9\pi}\right)^{1/3} - \frac{g d_b}{560 u_{\text{mf}} u_b} \tag{1}$$

where d_b, z, ε, u_{mf} and u_b stand respectively for bubble diameter, height along the bed, bed voidage, minimum fluidization velocity and bubble velocity. The Hilligardt−Werther correlation was developed for bubbling fluidized beds of Geldart Groups A and B particles and evaluated across laboratory- to meter-scale units spanning multiple bed geometries and superficial gas velocities. Experiments were conducted primarily at ambient conditions, with additional measurements extending to elevated temperatures (up to 930 °C); particle sizes were reported largely as nominal or mean values, without explicit characterization of continuous PSD widths. In contrast, the experimental data set shown in Figure 1 corresponds to a single laboratory-scale bubbling bed operated at ambient temperature, with explicitly prescribed continuous Gaussian and log-normal particle-size distributions spanning a wide range of PSD widths.

The Hilligardt and Werther correlation was adopted in this study for three main reasons. First, in contrast to other classical correlations, Hilligardt and Werther explicitly cast bubble growth in a differential form $\left(\frac{\mathrm{d}d_b}{\mathrm{d}z}\right)$, which aligns naturally with the PINN and UDE frameworks and enables direct embedding as a governing equation. Second, the correlation was developed using data sets that include Geldart Group B particles, making it well suited to the particles considered here. Third, the correlation explicitly expresses two competing mechanisms governing bubble evolution with height (namely, growth associated with coalescence and a counteracting term associated with bubble splitting) providing a physically interpretable decomposition that is particularly advantageous for UDE analysis, where the relative contributions of physics-aware terms and data-driven corrections are quantified. Although the Hilligardt−Werther correlation is empirical, it encodes a physically consistent bubble-growth trend; in this study it is therefore used as a physics-aware constraint rather than a first-principles governing law.

A PINN embeds known physical knowledge directly into the training objective of a neural network. Rather than learning mappings purely from data, the PINN incorporates the physics-informed differential relationship (in this case, the Hilligardt−Werther empirical correlation eq 1[17]) as a soft constraint by adding its residual to the loss function. Specifically, the loss penalizes the physics residual between the network-predicted derivative $\frac{\mathrm{d}d_\mathrm{b}}{\mathrm{d}z}$ (computed numerically via finite differences) and the right-hand side of eq 1, together with deviations from the initial condition (IC) at the lowermost bed height z_0 (i.e., the mean d_b value at z = 0.0508 m). This combination constrains the model to remain physically consistent and improves generalization with noisy data compared to purely data-driven models.

A PINN was compared against a purely data-driven NN to model bubble diameter d_b(z). Both models are multilayer perceptrons with tunable width, depth, and activation. To ensure a fair comparison and explore architectural sensitivity, random searches over key hyperparameters for each model family (hidden size, depth, activation, learning rate, and physics/IC weights for the PINN and L_2 weight decay for the NN). Training uses Adam optimizer with early stopping-style patience. The PINN objective is a weighted sum of physics-residual and IC terms, while the NN minimizes data mean-squared error (MSE).

Figure 4 compares the predictions of the black-box NN and the gray-box PINN for bubble diameter d_b as a function of fluidized bed height z for optimized hyperparameter sets. Also superimposed are predictions from the Hilligardt and Werther correlation (eq 1),[17] evaluated using an initial condition equal to the mean d_b at z = 0.0508 m. The boxplots represent the experimental distribution of bubble sizes at different axial positions, while the overlaid lines indicate the predicted trends from the two models, and the error bars represent the standard deviation, quantifying the models' epistemic uncertainty.

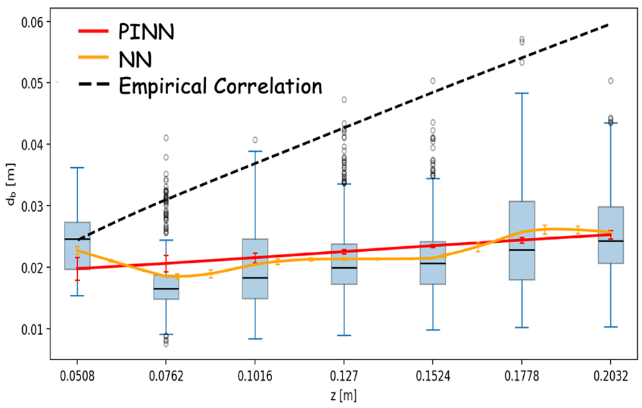

Figure 4. Comparing PINN and NN predictions on all data, with the error bars representing standard deviations of three runs. Also superimposed is the Hilligardt and Werther correlation (eq 1).[17]

In a BFB, bubbles tend to grow as they rise through the bed due to coalescence and gas expansion. For Geldart Group A particles, this happens quickly, up to an equilibrium maximum bubble diameter. On the other hand, for Geldart Group B, bubbles continue to grow throughout the fluidized bed height. The standalone empirical correlation overestimates bubble growth, illustrating the limitations of purely empirical models and motivating the use of hybrid approaches to generalize predictions beyond the experimental conditions used in their development. The PINN, constrained by the embedded empirical correlation, accurately reproduces the monotonic increase of d_b with z that is consistent with fundamental hydrodynamic behavior. Despite the mean d_b being uncharacteristically higher at the lowermost z (i.e., 0.0508 m) in the experiments, likely due to distributor effects, the PINN enforces fidelity with physical understanding and does not get affected by the "bad" data point. In contrast, the purely data-driven NN exhibits nonphysical fluctuations—predicting local decreases in d_b—despite being trained on the same data set. To verify robustness, the advantages conferred by the physics-aware trend enforcement in the PINN remain clear even when the lowest-height data are excluded. Due to the physical constraint, the MSE for the PINN ($5.2 \times 10^{-5} \pm 1.0 \times 10^{-7}$) is slightly higher than that of NN ($5.1 \times 10^{-5} \pm 1.3 \times 10^{-7}$).

This highlights the key advantage of physics-aware modeling: by incorporating governing equations with known physical relationships (e.g., $\frac{\mathrm{d}d_\mathrm{b}}{\mathrm{d}z} > 0$) into the loss function, the PINN enforces physically consistent behavior even when the data are noisy. Notably, although the embedded "governing equation" is an empirical correlation rather than derived from first-principles, its formulation captures the physical trend of bubble growth with height. This intrinsic physical description provides sufficient constraint to guide the model toward realistic predictions under data uncertainty conditions as in this case. Consequently, the PINN exhibits enhanced robustness and interpretability, ensuring that predictions adhere to the fundamental phenomenon that bubble size increases with bed height. To further understand the discrepancy between the empirical correlation and experimental data, a Universal Differential Equation (UDE) framework is employed for explicit decomposition of physics-based and data-driven contributions.

A UDE is a hybrid modeling framework that integrates known physics with data-driven corrections, expressed in a differential equation form as:

$$\frac{\mathrm{d}y}{\mathrm{d}t} = f_\mathrm{phys}(y, t, \theta_\mathrm{phys}) + g_\mathrm{NN}(y, t, \theta_\mathrm{NN}) \tag{2}$$

where f_phys is known physical law or empirical model, g_NN is neural correction term (learned from data), θ_phys are physical constants (possibly trainable), and θ_NN are NN parameters. When both components are trained jointly, the result is a UDE that combines the interpretability of physics-based models with the adaptability of machine learning. In contrast to PINNs, which embed fully known governing equations, UDEs assume that the physics is partially known and learn both physical and correction terms. This cotraining enables data-calibrated physical models that remain interpretable and predictive.

In this study, a UDE framework was implemented to model the evolution of the bubble diameter $d_\mathrm{b}(z)$ along the bed height z, combining physical knowledge with data-driven correction. The equation becomes

$$\frac{\mathrm{d}d_\mathrm{b}}{\mathrm{d}z} = \left(\frac{2\varepsilon}{9\pi}\right)^{1/3} - \frac{gd_\mathrm{b}}{560u_\mathrm{mf}u_\mathrm{b}} + \beta{\cdot}\mathrm{NN}(z, \varepsilon, u_\mathrm{b}) \tag{3}$$

where $f_\mathrm{phys}(d_\mathrm{b}, \varepsilon, u_\mathrm{b}) = \left(\frac{2\varepsilon}{9\pi}\right)^{1/3} - \frac{gD}{560u_\mathrm{mf}u_\mathrm{b}}$ represents the Hilligardt−Werther empirical correlation (eq 1), and NN-

(z,ε,u_b) is a neural network that captures data-driven dynamics. Experimental data were preprocessed, normalized, and used to train the UDE using PyTorch with a smooth L1 (Huber) loss combining data, physics, and initial-condition terms. The neural correction network and the learned scaling parameter β were optimized jointly via gradient descent using automatic differentiation. This approach enforces physical consistency while allowing flexible correction of discrepancies between the theoretical model and the experimental observations. Post-training, the model predicts $d_b(z)$ across the measurement domain and decomposes the total derivative into physical and neural contributions for interpretability.

Fitting eq 3 to the data, as depicted in Figure 5, gives a modest MSE of 8.2×10^{-4} and a β value of 0.28. This indicates that the learned correction term contributes 28% of the total correlation, while the empirical correlation component remains dominant. This result underscores the strong physical basis of the empirical model—even though it is not derived from first-principles—while the neural correction captures real-world deviations, such as those caused by nonideal flow conditions. Overall, this hybrid model is not merely a regression—it respects physical principles through f_{phys}, adapts to experimental data via the neural correction term (g_{NN}), and retains interpretability through explicit quantification of the correction magnitude (β). The resulting model is both physically consistent and data-informed, accurately capturing the increase of bubble size with bed height while refining the prediction through learned adjustments based on experimental observations.

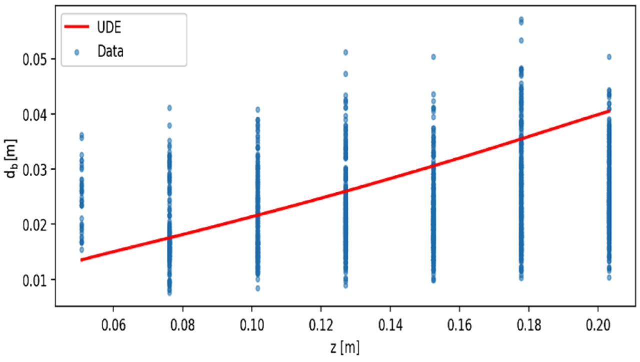

Figure 5. UDE marrying empirical correlation and neural-network correction.

Figure 6 illustrates the individual and combined contributions of the empirical (physics-based) term f_{phys} and the neural-network correction term g_{NN} to the overall bubble growth rate, $\frac{dd_b}{dz}$. The total derivative $\frac{dd_b}{dz}$ increases across the bed height, indicating that the learned model predicts increasing bubble diameter d_b with z. The empirical correlation contributes a positive term, reflecting the expected physical trend of bubble growth with height. Conversely, the neural correction term contributes a negative component, effectively counteracting the overprediction from the empirical model. Physically, this implies that the empirical correlation slightly overestimates bubble growth, and the data-driven NN compensates by applying an opposing correction. Although the two components nearly cancel, the global weighting parameter remains modest ($\beta = 0.28$). This does not indicate weak interaction; rather, the NN internally produces large-magnitude corrections that are scaled by the small β factor for numerical stability. The optimizer thus achieves balance not by equalizing term magnitudes but by tuning the product $\beta\cdot$NN to offset f_{phys} where necessary. Overall, the small value of β shows that the model trusts the physics-based correlation more strongly, using the neural component sparingly and locally to refine predictions. The result is a stable, interpretable hybrid model in which the neural term adjusts the empirical prediction only where data indicate systematic deviations.

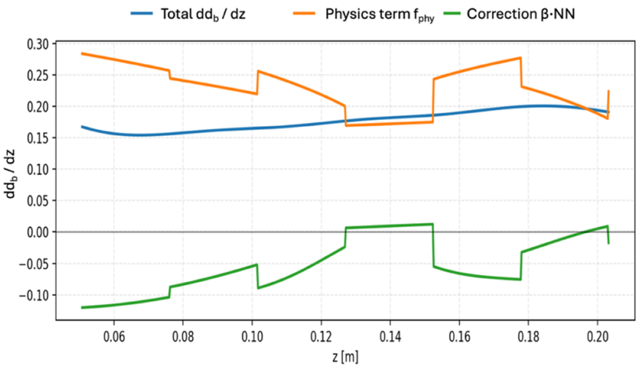

Figure 6. Relative contributions of the empirical correlation and neural-network correction in the UDE.

In the Hilligardt and Werther correlation (eq 1), four empirical fitting parameters were originally introduced to improve agreement with experimental data, but such empirical constants are well-acknowledged to lack generalizability beyond the data set used for the fitting. The UDE framework can be modified to learn the fitted empirical constants jointly with the neural correction, thereby relaxing structural biases in the empirical correlation tied to the data set used while retaining interpretability. In other words, the empirical constants can be flexibly adjusted within the UDE framework to further refine the model's predictive accuracy. In this formulation, the UDE can be expressed as

$$\frac{dd_b}{dz} = \left(\frac{a_1\varepsilon}{a_2\pi}\right)^{a_3} - \frac{gd_b}{a_4 U_{mf} U_b} + \beta\cdot\mathrm{NN}(z,\ \varepsilon,\ u_b) \tag{4}$$

where a_1–a_4 represent the learned empirical constants, and $\beta\cdot\mathrm{NN}(z,\varepsilon,u_b)$ is a data-driven correction term. Specifically, a_1, a_2, $a_4 > 0$ are enforced via softplus reparameterization and a_3 is constrained near the nominal 1/3 using a tanh-window around $a_{3,0} = 1/3$. The parameters z, ε, and u_b are normalized and a feedforward field network $d_b(z)$ is trained together with a NN correction and the learnable physics block (a_1, a_2, a_3, a_4). Training minimizes a composite objective: a Huber data-fit term for $d_b(z)$, an initial-condition penalty, a collocation-based physics residual that uses the chain rule to convert $\partial d_b/\partial z_{norm}$ to $\partial d_b/\partial z$, and a weak quadratic prior nudging (a_1, a_2, a_3, a_4) toward their nominal values $\left(2,\ 9,\ \frac{1}{3},\ 560\right)$. Parameters are optimized with Adam, with the outputs being the learned empirical constants and β. Together, these elements yield a data-informed recalibration of the Hilligardt–Werther correlation acting as the mechanistic model, quantify where the neural term is essential, and reveal how z, ε, and u_b drive the predicted bubble-diameter dynamics. This hybrid formulation preserves the physical structure of the original correlation while allowing the parameters and correction term to adapt to experimental data, thereby achieving a more accurate and

https://doi.org/10.1021/acs.iecr.5c05433
Ind. Eng. Chem. Res. 2026, 65, 7273−7286

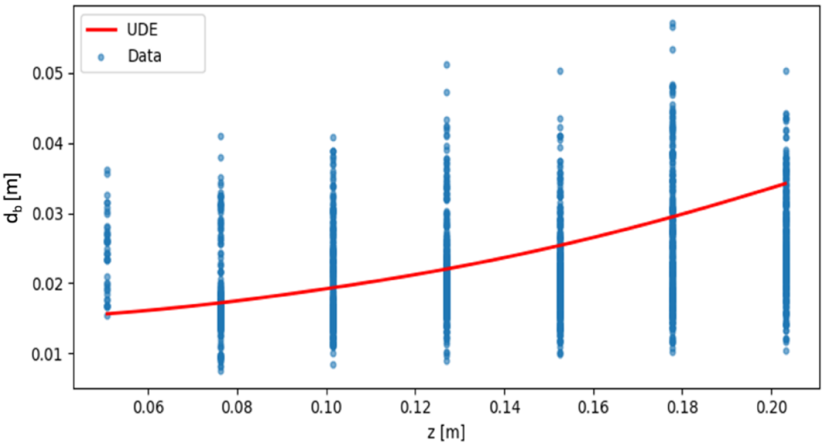

Figure 7. UDE with adjusted empirical constants.

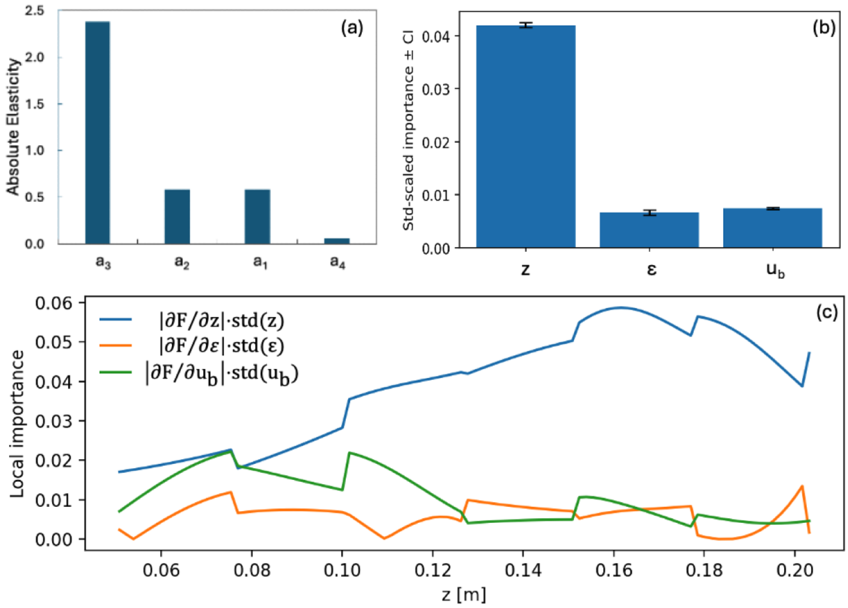

Figure 8. Sensitivity analysis of the UDE model with optimized empirical constants: (a) influence of empirical constants on β; (b) global sensitivity of parameters in empirical correlation with 95% confidence interval (CI); (c) local sensitivities along z.

physically consistent representation of bubble growth along the bed height.

Figure 7 illustrates the fitted UDE describing the evolution of bubble diameter d_b with bed height z, incorporating both learned physical constants and a NN correction term. The final learned equation is with parameters $a_1 = 1.99$, $a_2 = 9.00$, $a_3 = 0.33$, $a_4 = 556.1$, and $\beta = 0.20$. The learned constants remain remarkably close to the original empirical values, confirming that the Hilligardt-Werther correlation provides a robust physical description of bubble growth. The parameter a_1 remains nearly identical to its nominal value of 2.0, validating the voidage-evolution scaling, while $a_2 \approx 9.0$indicates that no correction is required for the normalization constant. The exponent $a_3 = 0.33$ is effectively one-third, reinforcing the cube-root dependence between voidage and bubble size. The learned parameter $a_4 = 556.1$, slightly below the original value of 560, suggests a marginal increase in the dominance of bubble breakup and thus implying that the empirical correlation slightly overpredicted bubble growth for this data set. Finally, the global scaling factor $\beta = 0.20$ shows that the neural correction contributes about 20% of the total trend amplitude, serving primarily as a fine-tuning mechanism rather than a dominant component. Between the original and adjusted empirical constants, the β values are respectively 0.28 and 0.20. The lower value associated with the latter indicates that the data-driven NN component plays a smaller role, which in turn implies that the recalibrated empirical correlation provides a stronger influence.

Regarding the influence of the empirical constants on β, elasticity $((a_n/\beta)\cdot(\partial\beta/\partial a_n))$ can be determined to quantify how sensitive β is to a percentage change in each constant. Figure 8a shows that β is most significantly affected by the exponent a_3, which exhibits a large negative elasticity (−2.38). This indicates that increasing a_3 markedly decreases β, implying that a higher voidage exponent reduces the model's reliance on data and enhances the dominance of the empirical correlation. The parameters a_1 and a_2 have moderate but opposing effects ($\approx\pm0.6$ elasticity), consistent with their roles in the numerator and denominator of the voidage-related term. In contrast, a_4 exerts only a minor influence (≈ 0.06) on β, suggesting the bubble splitting-related term in the empirical correlation contributes little to the balance between physics and data. This aligns with mechanistic expectations, as bubble coalescence tends to dominate over bubble breakup in the low-velocity bubbling fluidized bed regime, whereas breakup becomes more important in the higher-velocity regimes. Overall, β is governed primarily by the voidage-related term in the empirical correlation, especially the exponent a_3, while a_1 and a_2 provide secondary, roughly symmetric influences.

The results demonstrate that the physics-based component remains dominant: the empirical correlation captures the main bubble growth behavior, while the neural correction refines the model to account for subtle nonidealities in the experiments. The close alignment between the learned and nominal constants confirms that the underlying physics—particularly the cube-root law relating energy input to bubble size—holds strongly for the data set despite the noise. The small correction factor further indicates that the model predominantly relies on physical principles, invoking data-driven learning only where experimental deviations occur.

Figure 8b presents the global sensitivity analysis of the learned UDE. A permutation-importance analysis was performed, and bootstrap confidence intervals are determined for global sensitivities. The bar chart shows the global standardized sensitivities of the governing function $F(z,\varepsilon,u_\mathrm{b})$ with 95% confidence intervals, revealing that the bed height z has the strongest influence on model output. Its normalized sensitivity of 0.042 is approximately six times larger than those of voidage (0.0066) and bubble rise velocity (0.0074). The line plots in Figure 8c illustrate the local sensitivities along the bed height, showing that $\left|\frac{\partial F}{\partial z}\right|$ increases steadily with z, whereas the sensitivities to ε and U_b remain comparatively small and spatially variable. Regarding ε and U_b, the former is in the growth term while the latter is in the splitting term in the correlation (eq 1), so their influence depends on the local balance between these mechanisms as d_b evolves. Figure 8b,c confirm that bubble growth behavior is governed primarily by the axial position, consistent with the physical expectation that bubble size increases with height in a BFB. The strong dependence on z reflects both its direct role in the neural correction term and its indirect influence through $d_\mathrm{b}(z)$in the physics-based component of the UDE. Altogether, the sensitivity patterns demonstrate that the learned UDE functions as a calibrated hybrid model that respects the governing physics, adapts to experimental data through localized neural corrections, and remains fully interpretable and physically consistent.

Figure 9 further illustrates the internal balance between the empirical correlation and neural-network correction within the UDE. Compared to Figure 6, the rate of growth of bubbles with height $\left(\frac{\mathrm{d}d_\mathrm{b}}{\mathrm{d}z}\right)$ is more linear, reflecting the impact of the adjusted empirical constants. The total derivative $\frac{\mathrm{d}d_\mathrm{b}}{\mathrm{d}z}$ matches closely with the sum of the empirical term f_phys and the neural correction $\beta\cdot$NN, with a MSE of only 6.1×10^{-4}, which is slightly smaller than that with the original empirical constants (8.2×10^{-4}). This near-zero discrepancy indicates excellent internal consistency, confirming that the learned parameters yield an ODE that holds accurately across the entire data range. The empirical term is positive throughout the bed height, representing the expected trend of increasing bubble size with z, while the neural correction is smaller and generally negative, compensating for the empirical model's slight overprediction of bubble growth. Their near-cancellation results in a smooth total derivative curve that aligns with the experimental trend. The modest weighting factor ($\beta \approx 0.2$) shows that the model primarily relies on the physics-based governance, using the neural correction sparingly to account for localized deviations and nonidealities.

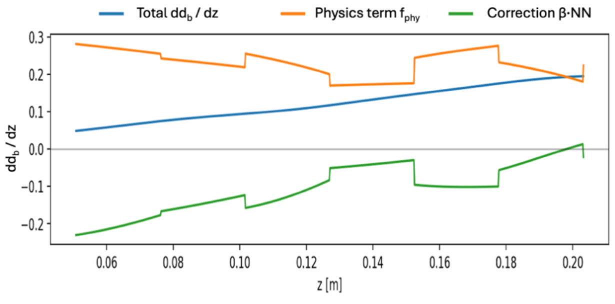

Figure 9. Relative contributions of the empirical correlation and neural-network correction in the UDE with learned empirical constants.

Gradient-based sensitivity analysis reinforces this interpretation: the mean magnitudes of the partial derivatives—$\left|\frac{\partial F}{\partial z}\right| = 0.96$, $\left|\frac{\partial F}{\partial \varepsilon}\right| = 0.08$, and $\left|\frac{\partial F}{\partial U_\mathrm{b}}\right| = 0.05$—indicate that the model response changes roughly one unit per unit variation in z, but only a tenth as much for ε or u_b. Bootstrap-based sensitivities (z: 0.0420 ± 0.0005, ε: 0.0066 ± 0.0005, u_b: 0.0074 ± 0.0002), derived by repeatedly resampling data using the bootstrap to assess how variations in the data affect the model's parameter estimates, confirm that these relative importances are statistically robust, with narrow confidence intervals and no overlap between z and the other variables. Permutation importance analysis produces similar error increases ($\Delta\text{error} \sim 1.3-1.4 \times 10^{-3}$) for all three inputs, suggesting that while z dominates in magnitude, the neural correction moderately integrates all inputs, capturing cross-effects between voidage and bubble velocity.

Taken together, these analyses show that the learned UDE achieves a stable and physically interpretable balance: the empirical correlation governs the main bubble growth dynamics, while the neural component provides targeted, data-driven adjustments that enhance quantitative accuracy. The model thus successfully reconciles physical realism with machine-learning flexibility, maintaining both predictive reliability and mechanistic interpretability.

To further challenge the hybrid model, subsets of the experimental data were employed. Our earlier unsupervised learning analysis revealed that variations in the particle-size distributions (PSDs) within the bed govern the grouping of bubble data into distinct data assemblies.[21] Specifically, the log-normal PSD with a standard deviation-to-Sauter mean diameter ratio (σ/d_sm) of 10% exhibited distinctly different bubble characteristics compared to those for a broader log-normal PSD of 70%. These contrasting subdata sets provide an ideal basis for evaluating the generalizability and robustness of the hybrid model formulations.

For the bed with the PSD width of 10%, both the PINN and UDE were evaluated to assess model fidelity and internal consistency. For this data set, bubbles were not detectable at $z = 0.0508$ m.[34] The comparison between the PINN and a purely data-driven NN in Figure 10 shows that, while both models capture the overall distribution of bubble diameters

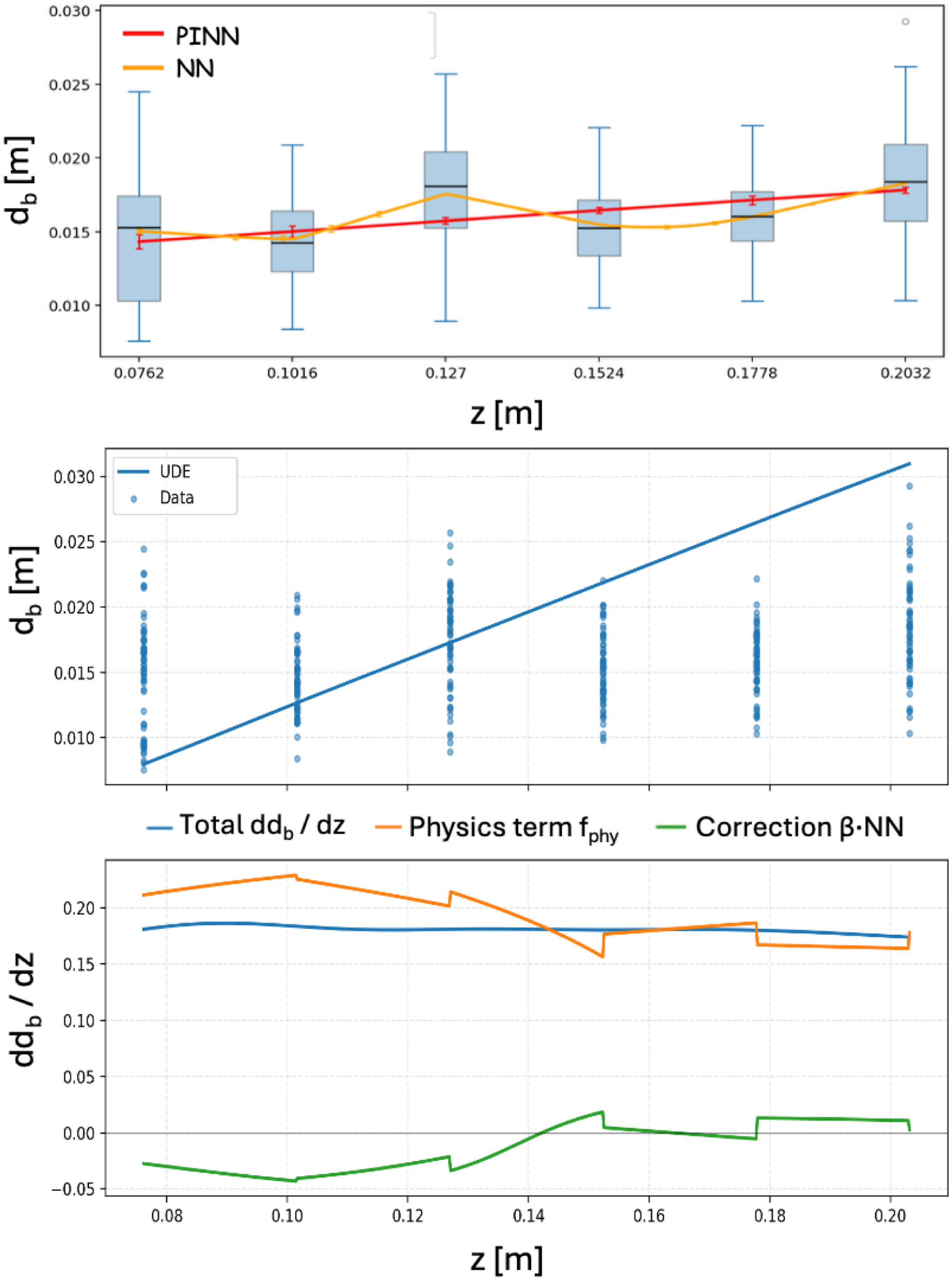

Figure 10. PINN and UDE performance and UDE decomposition for PSD with σ/d_{sm} = 10%.

(d_b) across bed height (z), the PINN preserves the expected physical monotonicity of increasing d_b with z. The NN, in contrast, exhibits mild nonphysical undulations despite achieving a slightly lower mean squared error (MSE = $1.1 \times 10^{-5} \pm 1.9 \times 10^{-8}$) compared to the PINN ($1.2 \times 10^{-5} \pm 2.4 \times 10^{-7}$). This highlights the typical trade-off between predictive accuracy and physical consistency.

Furthermore, Figure 10 presents the UDE fit and derivative decomposition for the same data set. The learned UDE equation successfully balances the empirical (physics-based) term f_{phys} with the learned correction term β_{10}·NN, with a global weighting factor of β_{10} = 0.25, which is slightly less than that for the overall data set (β = 0.28) and indicates that the empirical correlation is somewhat more descriptive of the narrow PSD. The small mean absolute residual between the total derivative $\frac{dd_b}{dz}$ and the sum of both components (8.6×10^{-4}) demonstrates excellent internal consistency, confirming that the trained model satisfies the governing differential relationship across the domain. The average magnitudes of the contributing terms further reveal the near-perfect balance between the physics and learned components, with the mean of f_{phys} being 0.194 and the mean of β_{10}·NN being −0.0195,

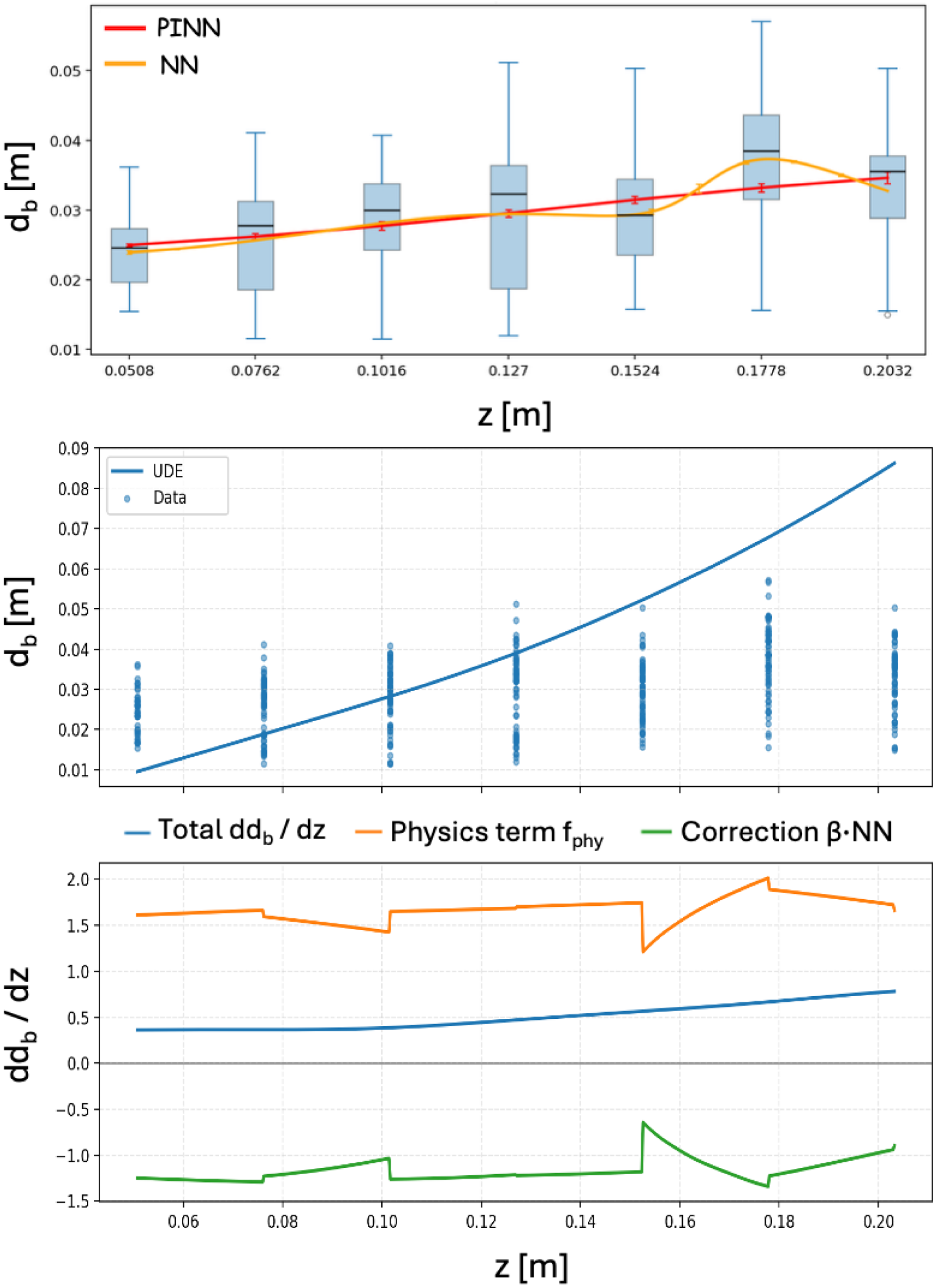

Figure 11. PINN and UDE performance and UDE decomposition for PSD with σ/d_{sm} = 70%.

giving the mean of $\frac{dd_b}{dz}$ as 0.181. The order-of-magnitude larger magnitude of f_{phys} relative to β·NN indicates the physical relevance of the empirical correlation dominates, while the opposite signs of f_{phys}(positive) and β_{10}·NN(negative) indicate that the neural correction assists in compensating for the overprediction of bubble growth by the empirical correlation to align the overall trend with the observed data. In physical terms, this balance reflects a self-consistent hybrid model in which the empirical component dictates the primary bubble growth dynamics, while the neural correction locally refines the prediction by counteracting overestimated growth rates. The result is a physically faithful and numerically stable model that reconciles data fidelity with hydrodynamic realism for the narrow PSD (σ/d_{sm} = 10%) case.

For the particle system with a log-normal PSD with σ/d_{sm} = 70%, bubble diameters are generally larger. The comparison between the PINN and the data-driven NN in Figure 11 shows that, while both models approximate the general distribution of bubble diameters (d_b) along the bed height (z), the PINN enforces a monotonic increase of d_b with z. The purely data-driven NN similarly achieves a slightly lower mean squared error (MSE = $6.3 \times 10^{-5} \pm 1.2 \times 10^{-8}$) compared to the PINN ($6.7 \times 10^{-5} \pm 1.6 \times 10^{-7}$), reflecting its greater flexibility in capturing the complex dynamics introduced by the broader PSD. However, the NN lacks the physical governance and interpretability that the hybrid framework provides. Figure 11 also shows the UDE fit and derivative decomposition. The learned hybrid model exhibits strong internal consistency, with a mean residual between the total derivative $\mathrm{d}d_b/\mathrm{d}z$ and the sum of the physics and learned correction terms of 2.3×10^{-3}. The UDE thus satisfies its governing differential form with high precision across the data domain, even under the more challenging data associated with this broader PSD, since the PSD used to develop the Hilligardt−Werther correlation was likely not so broad. The fitted global weighting factor (β_{70} = 0.35) is noticeably higher than that for the narrower PSD with σ/d_{sm} = 10% (β_{10} = 0.25) and overall (β = 0.28) cases, indicating that the empirical correlation becomes less representative as particle polydispersity increases and that the neural correction plays a stronger compensatory role. The mean magnitudes of the components further highlight this balance, with the mean of f_{phys} being 1.67 and the mean of $\beta_{70}\cdot$NN being −1.17, giving the mean of $\frac{\mathrm{d}d_b}{\mathrm{d}z}$ as 0.50. Here, the empirical term f_{phys} is approximately equal in magnitude as the neural correction term $\beta_{70}\cdot$NN. This near-symmetric balance indicates that the UDE relies heavily on the learned correction to counteract the empirical model's overestimation of bubble growth in the broad-PSD case. Physically, the larger data-driven corrective contribution reflects that the empirical correlation is less able to describe bubble evolution in a highly polydisperse system. The neural term thus acts to modulate the correlation dynamically, introducing spatially varying corrections that preserve numerical stability while improving fit to experimental observations. Importantly, although the correction becomes comparable to the empirical term, the model remains physics-aware rather than reverting to a black-box regression because the empirical differential equation is retained and the neural network plays only the role of a constrained additive correction. In summary, for the 70% PSD, the UDE captures the essential bubble growth trends while adaptively compensating for the empirical model's reduced validity for the highly polydisperse particle system. The increased β_{70} value underscores the model's flexibility: as the representativeness of the underlying physics diminishes, the data-driven component autonomously assumes a larger but still physically constrained role, maintaining overall consistency between the data-learned and empirical-correlation dynamics.

A comparison between the 10% and 70% PSDs reveals how increasing polydispersity influences the relative contributions of the physics-based and neural components in the UDE framework. For the narrow 10% PSD, the empirical correlation provides a more accurate physical basis, with the UDE requiring only a modest neural correction ($\beta_{10} \approx 0.25$) to reconcile minor data deviations from the correlation. The physics and correction terms (f_{phys} and $\beta\cdot$NN) are an order of magnitude apart, indicating a subtle damping of over-predictions by the empirical correlation. The model maintains excellent internal consistency (MSE ~ 8.6×10^{-4}) and physical fidelity, confirming that the underlying correlation remains robust under conditions of low particle-size variability. In contrast, the 70% PSD case exposes the empirical model's limitations in representing bubble behavior in highly polydisperse systems. The broader PSD produces more complex, nonmonotonic bubble dynamics that the original correlation alone cannot fully capture. Specifically, empirical correlations, including the Hilligardt−Werther formulation, are typically calibrated using relatively narrow PSDs. As PSD width increases, particle-size segregation and voidage heterogeneity become more pronounced, modifying local bubble coalescence and breakup and thereby increasing deviations from the empirical correlation. Consequently, the learned weighting factor increases to $\beta_{70} \approx 0.35$, signifying greater reliance on the neural correction. The higher learned correction β for the broader PSD width indicates that polydispersity is a dominant contributor to deviations from the empirical correlation, whereas operating-condition effects are less influential because these dependencies are already embedded in the empirical correlation (eq 1). Here, the correction term is nearly equal in magnitude—but oppositely in sign—to the empirical term, effectively counteracting systematic overestimation of bubble growth. Despite this stronger data-driven influence, the UDE remains internally consistent (MSE ~ 2.3×10^{-3}) and physically interpretable, preserving stability while adapting to local deviations.

Overall, the results demonstrate that as the PSD broadens, the empirical correlation's dominance gradually diminishes, and the neural correction assumes a more active role in maintaining model accuracy. The UDE framework thus dynamically rebalances its physics- and data-driven components according to the degree of error via the correlation, ensuring predictive robustness while retaining mechanistic transparency. This adaptive interplay underscores the potential of UDEs to generalize across regimes where traditional empirical correlations lose validity, without sacrificing physical interpretability. Notably, it also highlights the possibility of judiciously using existing well-thought-through correlations toward reliable predictions while first-principles-based governing equations remain elusive.

Accurate prediction of bubble diameter has direct implications for reactor efficiency and design of bubbling fluidized beds. Bubble size governs interphase mass and heat transfer, and solids circulation. Error in predicted bubble size propagates into design calculations: overpredicting bubble diameter typically implies higher bubble rise velocities, which can lead to underestimation of gas residence time and, consequently, overestimation of the required bed height (i.e., reactor oversizing); the opposite follows from underprediction. By enforcing physically consistent bubble-growth trends while remaining data-adaptive, the proposed PINN and UDE frameworks yield more reliable bubble-evolution profiles. This is particularly important when applying empirical correlations beyond their calibration range, for example in beds with broad PSDs.

5. CONCLUSION

This study presents a hybrid modeling framework to modeling bubble growth dynamics in a bubbling fluidized bed through the integration of physical constraints via the empirical Hilligardt−Werther correlation[17] and data-driven learning to account for nonidealities associated with practical data. Experimental bubble data used for training are characteristically noisy with non-normal bubble diameter distributions. Two complementary hybrid (gray-box) models, namely, Physics-Informed Neural Network (PINN) and Universal Differential Equation (UDE), were implemented.

The PINN, constrained by an embedded empirical correlation, successfully enforced the physically consistent monotonic increase of bubble diameter with bed height, while the purely data-driven neural network (NN) occasionally violated this constraint despite achieving a lower mean squared error. The UDE extended this approach by coupling the same empirical correlation with a learned neural correction term to achieve a balance between physical interpretability and data adaptability. The hybrid formulation allowed simultaneous learning of empirical constants and correction weights, enabling the model to remain both physically grounded and data calibrated. The results demonstrate that the empirical correlation provided a robust physical foundation, with the UDE maintaining internal consistency (mean residual on the orders of 10^{-3} to 10^{-4}) across all cases. The global weighting factor, β, quantified the relative contribution of the neural correction: $\beta_{10} \approx 0.25$ for the narrow PSD ($\sigma/d_{\mathrm{sm}} = 10\%$) and $\beta_{70} \approx 0.35$ for the broad PSD ($\sigma/d_{\mathrm{sm}} = 70\%$). These values indicate that while the empirical correlation predominates, the data-driven correction becomes increasingly influential as PSD broadens. The learned model thus adaptively rebalanced the contributions of physical governance and data-driven components, preserving physical realism while compensating for limitations of the empirical correlation. Sensitivity analyses further confirmed that bed height (z) remains the most influential variable, with voidage (ε) and bubble velocity (u_b) exerting secondary but coupled effects through the neural correction term. Collectively, the hybrid models captured the key physical trends while maintaining numerical stability, interpretability, and agreement with noisy experimental data.

Future work can focus on extending the PINN and UDE framework to include spatiotemporal dynamics and multiphase coupling beyond one-dimensional height dependence. Incorporating time-resolved bubble tracking data and additional hydrodynamic measurements (e.g., pressure fluctuations) would potentially allow a more comprehensive description of bubble behaviors. Furthermore, integrating uncertainty quantification and Bayesian calibration could enhance the interpretability and reliability of learned corrections, especially when extrapolating beyond training conditions. Finally, expanding the data set to encompass a broader range of particle sizes and PSDs, bed geometries, and operating conditions would enable more robust generalization of the physics-consistent hybrid model, facilitating predictive design and optimization of fluidized-bed reactors. Notably, the gray-box nature of such models substantially reduces the amount of data required for effective training and deployment.

From a reactor-design perspective, accurate prediction of bubble growth improves estimation of interphase mass and heat transfer, bed expansion, and reaction rates, all of which are pivotal to reactor efficiency and scale-up decisions. The physics-aware (gray-box) framework presented here reduces reliance on empirical correlations applied beyond their original calibration scope, while also avoiding the nonphysical behavior that can arise in purely data-driven models. Correspondingly, the approach provides a more reliable basis for reactor sizing, which is valuable for expediting scale-up by reducing design uncertainty.

■ AUTHOR INFORMATION

Corresponding Author

Jia Wei Chew − *Department of Chemistry and Chemical Engineering, Chalmers University of Technology, Gothenburg 412 96, Sweden;* orcid.org/0000-0002-6603-1649; Email: jia.chew@chalmers.se

Authors

Ronnie Andersson − *Department of Chemistry and Chemical Engineering, Chalmers University of Technology, Gothenburg 412 96, Sweden;* orcid.org/0000-0002-2838-6115

Ray A. Cocco − *Particles in Motion, LLC, Elmhurst, Illinois 60126, United States*

Complete contact information is available at:
https://pubs.acs.org/10.1021/acs.iecr.5c05433

Notes

The authors declare no competing financial interest.

■ ACKNOWLEDGMENTS

J.W.C. acknowledges funding from Chalmers Gender Initiative for Excellence (Genie).

■ REFERENCES

(1) Kunii, D.; Levenspiel, O. CHAPTER 2 - Industrial Applications of Fluidized Beds. In *Fluidization Engineering*; 2nd ed., Butterworth-Heinemann: Oxford, United Kingdom; 1991, pp. 15−59.

(2) Leckner, B. From bubbling to circulating fluidized bed combustion—development and comparison. *Heliyon* **2024**, *10* (13), No. e33415.

(3) Koornneef, J.; Junginger, M.; Faaij, A. Development of fluidized bed combustion—An overview of trends, performance and cost. *Prog. Energy Combust. Sci.* **2007**, *33* (1), 19−55.

(4) Rüdisüli, M.; Schildhauer, T. J.; Biollaz, S. M. A.; van Ommen, J. R. Scale-up of bubbling fluidized bed reactors — A review. *Powder Technol.* **2012**, *217*, 21−38.

(5) Abdelmotalib, H. M.; Youssef, M. A. M.; Hassan, A. A.; Youn, S. B.; Im, I.-T. Heat transfer process in gas−solid fluidized bed combustors: A review. *Int. J. Heat Mass Transfer* **2015**, *89*, 567−575.

(6) Zhang, K.; Zhu, Y.; Jin, H.; Wang, S.; Wang, L. Multiscale analysis of flow behavior of bubbling fluidized bed with clouded bubble. *Adv. Powder Technol.* **2024**, *35* (6), 104498.

(7) Karimipour, S.; Pugsley, T. A critical evaluation of literature correlations for predicting bubble size and velocity in gas−solid fluidized beds. *Powder Technol.* **2011**, *205* (1), 1−14.

(8) Zhu, X.; Xu, Y.; Tu, Q.; Che, H.; Wang, H. Advanced measurement techniques for gas-solids fluidized beds in the power and energy industry - A review. *Meas.: Energy* **2024**, *4*, 100030.

(9) Errigo, M.; Lettieri, P.; Materazzi, M. X-ray imaging techniques for gas−solid fluidized beds: A technical review. *Particuology* **2025**, *101*, 67−89.

(10) Wang, H.; Yang, W. Application of electrical capacitance tomography in pharmaceutical fluidised beds – A review. *Chem. Eng. Sci.* **2021**, *231*, 116236.

(11) Yan, D.; Li, H.; Zhu, Q.; Zou, Z. Theoretical analysis and numerical simulation of the gas-solid hydrodynamics in pressurized bubbling fluidized beds. *Powder Technol.* **2025**, *455*, 120789.

(12) Xie, Y.; Chen, Y.; Fang, Z.; Zhou, H.; Wei, S.; Yang, L. The research of gas-solid fluidized bed bubbling behavior based on CFD-DEM coupled simulation. *Chem. Eng. Res. Des.* **2023**, *195*, 166−180.

(13) de Munck, M. J. A.; van Gelder, J. B.; Peters, E. A. J. F.; Kuipers, J. A. M. A detailed gas-solid fluidized bed comparison study on CFD-DEM coarse-graining techniques. *Chem. Eng. Sci.* **2023**, *269*, 118441.

(14) Darton, R. C.; Lanauze, R. D.; Davidson, J. F.; Harrison, D. Bubble Growth Due To Coalescence in Fluidized Beds. *Trans. Inst. Chem. Eng.* **1977**, *55*, 274−280.

(15) Mori, S.; Wen, C. Y. Estimation of bubble diameter in gaseous fluidized beds. *AIChE J.* **1975**, *21* (1), 109−115.

(16) Horio, M.; Nonaka, A. A generalized bubble diameter correlation for gas-solid fluidized beds. *AIChE J.* **1987**, *33* (11), 1865−1872.

(17) Hilligardt, K.; Werther, J. Influence of Temperature and Properties of Solids on the Size and Growth of Bubbles in Gas Fluidized Beds. *Chem. Eng. Technol.* **1987**, *10*, 272−280.

(18) Wytrwat, T.; Yazdanpanah, M.; Heinrich, S. Bubble Properties in Bubbling and Turbulent Fluidized Beds for Particles of Geldart's Group B. *Processes* **2020**, *8*, 1098.

(19) Jiang, S.; Wu, K.; Francia, V.; Ouyang, Y.; Coppens, M.-O. Machine Learning Assisted Experimental Characterization of Bubble Dynamics in Gas−Solid Fluidized Beds. *Ind. Eng. Chem. Res.* **2024**, *63* (19), 8819−8832.

(20) Liu, Y.; Wang, C.; Li, S. Comparative study of deep learning techniques for predicting bubble dynamics in a gas-solid fluidized bed. *Particuology* **2025**, *104*, 28−41.

(21) Chew, J. W.; Cocco, R. A. Effect of polydispersity on bubble characteristics of Geldart Group B particles. *Chem. Eng. J.* **2021**, *420*, 129880.

(22) Jaiswal, R.; Agu, C. E.; Nielsen, H. K.; Eikeland, M. S.; Emilie Moldestad, B. M.; Thapa, R. K. Investigation of Bubble Properties in a Bubbling Fluidized-Bed Gasification Reactor Using a Computational Particle Fluid Dynamic Model. *Ind. Eng. Chem. Res.* **2023**, *62* (21), 8500−8514.

(23) Li, S.; Yang, R.; Wang, C.; Han, H.; Shen, S.; Wang, H. CFD−PBM Simulation on Bubble Size Distribution in a Gas−Liquid−Solid Flow Three-Phase Flow Stirred Tank. *ACS Omega* **2022**, *7* (2), 1934−1942.

(24) van Wachem, B. G. M.; Schouten, J. C.; Krishna, R.; van den Bleek, C. M. Eulerian simulations of bubbling behaviour in gas-solid fluidised beds. *Comput. Chem. Eng.* **1998**, *22*, S299−S306.

(25) Chew, J. W.; Cahyadi, A.; Hrenya, C. M.; Karri, R.; Cocco, R. A. Review of entrainment correlations in gas−solid fluidization. *Chem. Eng. J.* **2015**, *260*, 152−171.

(26) Anantharaman, A.; Cocco, R. A.; Chew, J. W. Evaluation of correlations for minimum fluidization velocity (Umf) in gas-solid fluidization. *Powder Technol.* **2018**, *323*, 454−485.

(27) Chew, J. W.; Cocco, R. A. Application of machine learning methods to understand and predict circulating fluidized bed riser flow characteristics. *Chem. Eng. Sci.* **2020**, *217*, 115503.

(28) Gosavi, A. A.; Nandgude, T. D.; Mishra, R. K.; Puri, D. B. Exploring the Potential of Artificial Intelligence as a Facilitating Tool for Formulation Development in Fluidized Bed Processor: a Comprehensive Review. *AAPS Pharm. Sci. Technol.* **2024**, *25* (5), 111.

(29) Rackauckas, C.; Ma, Y.; Martensen, J.; Warner, C.; Zubov, K.; Supekar, R.; Skinner, D.; Ramadhan, A.; Edelman, A. Universal differential equations for scientific machine learning. *arXiv*, **2020**.

(30) Raissi, M.; Perdikaris, P.; Karniadakis, G. E. Physics-informed neural networks: A deep learning framework for solving forward and inverse problems involving nonlinear partial differential equations. *J. Comput. Biophys. Chem.* **2019**, *378*, 686−707.

(31) Iannello, S.; Friso, A.; Galvanin, F.; Materazzi, M. A Hybrid Physics−Machine Learning Approach for Modeling Plastic−Bed Interactions during Fluidized Bed Pyrolysis. *Energy Fuels* **2025**, *39* (9), 4549−4564.

(32) Li, X.; Wang, S.; Lin, J.; Luo, K.; Fan, J. Active control of bubbling fluidized bed by coupling deep reinforcement learning with reduced-order model. *Chem. Eng. Sci.* **2026**, *325*, 123353.

(33) Yang, P.; Guo, Q.; Chen, H. Deep learning assisted characterization of bubble behavior in a gas-solid fluidized bed with binary particle mixtures. *Powder Technol.* **2024**, *448*, 120333.

(34) Chew, J. W.; Hrenya, C. M. Link between bubbling and segregation patterns in gas-fluidized beds with continuous size distributions. *AIChE J.* **2011**, *57* (11), 3003−3011.